Supplementary Material — JPEG Anti-Forensics with Improved Trade-off between Forensic Undetectability and Image Quality

Wei Fan, Kai Wang, François Cayre, and Zhang Xiong

This Supplementary Material is organized as follows. Sec. 1 shows why we set $\alpha = 1.5$[1] in the first-round TV-based deblocking. The p.m.f. of the rounded dithering signal when the Laplacian model is used is calculated in Sec. 2. In Sec. 3, the constraints that λ_b should satisfy are described. Sec. 4 shows some example DCT histogram results of our JPEG forgery. The two intermediate images generated during our JPEG forgery creation process are compared with the JPEG image and our final JPEG forgery in Sec. 5. Finally, Secs. 6-7 present and compare the experimental results for hiding traces of aligned double JPEG compression, and for fooling JPEG artifact based image forgery localization, respectively, using JPEG anti-forensics.

1 Choosing the value for parameter α in the first-round TV-based deblocking

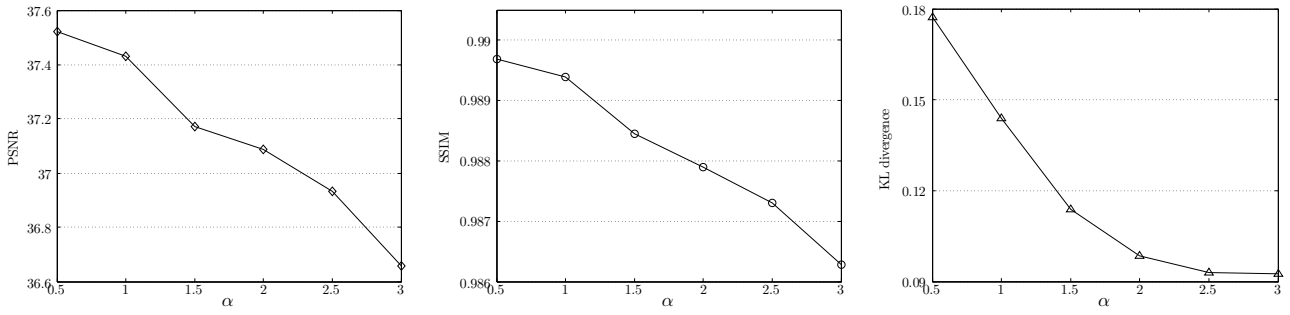

Figure 1: The quality and KL divergence change of the image after the first-round TV-based deblocking for different values of α. The uncompressed image is used as the reference for computing the metric values. Results are achieved by test on UCID92.

In order to select a good value for α (see the Eq. (8) in the paper) in the first-round TV-based deblocking, we create a set of intermediate images $\hat{\mathcal{F}}_b$ for comparison. The test is conducted on UCID92. Each UCID92 image is JPEG compressed with a quality factor selected from $\{50, 51, \cdots, 95\}$, and every two images have the same quality factor. Then the processed images $\hat{\mathcal{F}}_b$ are generated from the JPEG images for different values of α ranging from 0.5 to 3 with step 0.5.

As the first intermediate image during our JPEG anti-forensic image creation, the output of the JPEG forensic detectors is not taken into account for comparison now. We hope $\hat{\mathcal{F}}_b$ to have a good image quality and to recover as much DCT-domain information as possible for the consideration of the further perceptual DCT histogram smoothing. From Figure 1-(a) to -(c), the average PSNR, SSIM, and KL divergence values are respectively compared for different values of α. Note that all the metric values are computed using the uncompressed image as the reference. We can see that the image quality, as well as the KL divergence, decreases as α increases. When $\alpha > 2.5$, the curve of the average KL divergence trends to be flat. We therefore only consider $\alpha \leq 2.5$, as a high value of α will degrade too much the quality of the processed image, with limited improvement on the KL divergence. In the end, we choose $\alpha = 1.5$ as it appears to have a good trade-off between the DCT histogram restoration quality (which will contribute to the perceptual DCT histogram smoothing described in the Sec. IV-B of the paper) and the quality of the processed image.

[1] In this Supplementary Material, we may employ some notations or references in the paper without explanations, for the sake of simplicity. Please refer to the paper for the details.

2 Calculating the p.m.f. of the rounded dithering signal when the Laplacian model is used

Here, we only consider AC components of the image. The probability density function (p.d.f.) of the distribution of the dithering signal N is denoted as $P(N=n|Y=y)$. P can be easily computed (please refer to the Eqs. (13)-(15) in the paper for more information) according to the sign of the quantized DCT coefficient Y. Here, the probability mass functions (p.m.f.) of the rounded dithering signal are calculated with domain defined as the integer set $\{-\lfloor\frac{Q_{r,c}}{2}\rfloor, -\lfloor\frac{Q_{r,c}}{2}\rfloor+1, \cdots, \lfloor\frac{Q_{r,c}}{2}\rfloor\}$. Eqs. (1)-(2) below are the p.m.f. of the rounded dithering signal for quantization bin 0 when $Q_{r,c}$ is an odd number and an even number, respectively. For quantization bin $b \neq 0$, the p.m.f. of the rounded dithering signal are listed in Eqs. (3)-(6) according to the sign and the parity of b.

$$P_m^o(N=n|Y=0) = \begin{cases} 2c_0\lambda^{-1}\left(1-e^{-\lambda/2}\right) & \text{if} \quad n=0 \\ -c_0\lambda^{-1}e^{-\lambda(n+1/2)}\left(1-e^{\lambda}\right) & \text{if} \quad n=1,\cdots,\lfloor\frac{Q_{r,c}}{2}\rfloor \\ c_0\lambda^{-1}e^{\lambda(n+1/2)}\left(1-e^{-\lambda}\right) & \text{if} \quad n=-\lfloor\frac{Q_{r,c}}{2}\rfloor,\cdots,-1 \\ 0 & \text{otherwise,} \end{cases} \tag{1}$$

$$P_m^e(N=n|Y=0) = \begin{cases} 2c_0\lambda^{-1}\left(1-e^{-\lambda/2}\right) & \text{if} \quad n=0 \\ -c_0\lambda^{-1}e^{-\lambda Q_{r,c}/2}\left(1-e^{\lambda/2}\right) & \text{if} \quad n=-\frac{Q_{r,c}}{2},\frac{Q_{r,c}}{2} \\ -c_0\lambda^{-1}e^{-\lambda(n+1/2)}\left(1-e^{\lambda}\right) & \text{if} \quad n=1,\cdots,\frac{Q_{r,c}}{2}-1 \\ c_0\lambda^{-1}e^{\lambda(n+1/2)}\left(1-e^{-\lambda}\right) & \text{if} \quad n=-\frac{Q_{r,c}}{2}+1,\cdots,-1 \\ 0 & \text{otherwise,} \end{cases} \tag{2}$$

$$P_m^o(N=n|Y=y,y>0) = \begin{cases} -c_1\lambda^{-1}e^{-\lambda(n+1/2)}\left(1-e^{\lambda}\right) & \text{if} \quad n=-\lfloor\frac{Q_{r,c}}{2}\rfloor,\cdots,\lfloor\frac{Q_{r,c}}{2}\rfloor \\ 0 & \text{otherwise,} \end{cases} \tag{3}$$

$$P_m^e(N=n|Y=y,y>0) = \begin{cases} c_1\lambda^{-1}e^{\lambda Q_{r,c}/2}\left(1-e^{-\lambda/2}\right) & \text{if} \quad n=-\frac{Q_{r,c}}{2} \\ -c_1\lambda^{-1}e^{-\lambda Q_{r,c}/2}\left(1-e^{\lambda/2}\right) & \text{if} \quad n=\frac{Q_{r,c}}{2} \\ -c_1\lambda^{-1}e^{-\lambda(n+1/2)}\left(1-e^{\lambda}\right) & \text{if} \quad n=-\frac{Q_{r,c}}{2}+1,\cdots,\frac{Q_{r,c}}{2}-1 \\ 0 & \text{otherwise,} \end{cases} \tag{4}$$

$$P_m^o(N=n|Y=y,y<0) = \begin{cases} c_1\lambda^{-1}e^{\lambda(n+1/2)}\left(1-e^{-\lambda}\right) & \text{if} \quad n=-\lfloor\frac{Q_{r,c}}{2}\rfloor,\cdots,\lfloor\frac{Q_{r,c}}{2}\rfloor \\ 0 & \text{otherwise,} \end{cases} \tag{5}$$

$$P_m^e(N=n|Y=y,y<0) = \begin{cases} -c_1\lambda^{-1}e^{-\lambda Q_{r,c}/2}\left(1-e^{\lambda/2}\right) & \text{if} \quad n=-\frac{Q_{r,c}}{2} \\ c_1\lambda^{-1}e^{\lambda Q_{r,c}/2}\left(1-e^{-\lambda/2}\right) & \text{if} \quad n=\frac{Q_{r,c}}{2} \\ c_1\lambda^{-1}e^{\lambda(n+1/2)}\left(1-e^{-\lambda}\right) & \text{if} \quad n=-\frac{Q_{r,c}}{2}+1,\cdots,\frac{Q_{r,c}}{2}-1 \\ 0 & \text{otherwise.} \end{cases} \tag{6}$$

3 The constraints used for modeling the DCT coefficients

In the paper, for building the *adaptive local* dithering signal model for AC components, we combine the Laplacian model and the uniform model together. A key point to establish the adaptive local model for the dithering signal is that we try to find an appropriate parameter λ_b of the Laplacian model for each quantization bin b. If we cannot find a valid value for λ_b, the uniform model is used instead for the current and following quantization bin(s). The parameter λ_b is derived by solving a constrained weighted least-squares fitting problem (the Eq. (12) in the paper), with λ_b bounded between λ_b^- and λ_b^+. In the paper, we show how to search for the bound λ_b^+ (λ_b^- is set as 10^{-3}) for quantization bin 0 when $Q_{r,c}$ is an odd number, using a numerical method. Here we explain how to search for the two bounds in other cases.

3.1 In the quantization bin 0 when $Q_{r,c}$ is an even number

The empirical observation tells us that in the distribution of DCT coefficients of AC component, the probability of DCT coefficient decreases when the coefficient magnitude increases. Now we consider the quantization bin 0 when $Q_{r,c}$ is an even number.

As illustrated in Figure 2, the probability of DCT coefficient falling in the leftmost (or rightmost) integer bin should be no smaller than either that in the rightmost integer bin of quantization bin -1 or that in the leftmost integer bin of quantization bin 1. For the moment, the neighboring quantization bins -1 and 1 are

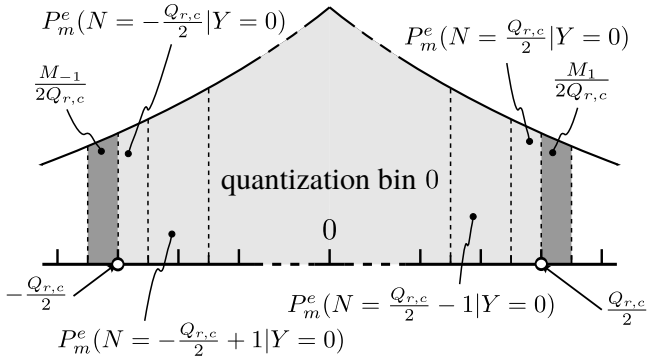

Figure 2: For the quantization bin 0, the probability of DCT coefficient falling in the leftmost (or rightmost) integer bin should be no smaller than either that in the rightmost integer bin of quantization bin -1 or that in the leftmost integer bin of quantization bin 1.

assumed to follow a uniform distribution. Similarly to the case in the quantization bin 0 when $Q_{r,c}$ is an odd number, we still set $\lambda_b^- = 10^{-3}$, whereas λ_b^+ can be found by solving:

$$\lambda_b^+ = \underset{10^{-3}\le\lambda\le 1}{\arg\max}\ \lambda,\ \text{subject to: } P_m^e\left(N=\tfrac{Q_{r,c}}{2}-1|Y=0\right)\times M_0 \ge P_m^e\left(N=\tfrac{Q_{r,c}}{2}|Y=0\right)\times M_0 + \tfrac{1}{2}\max\left(\tfrac{M_{-1}}{Q_{r,c}},\tfrac{M_1}{Q_{r,c}}\right), \tag{7}$$

using a numerical method. Note that M_b ($b = B_{r,c}^-, B_{r,c}^- + 1, \cdots, B_{r,c}^+$) denotes the approximate probability that the DCT coefficient falls in quantization bin b.

3.2 In the quantization bin $b > 0$

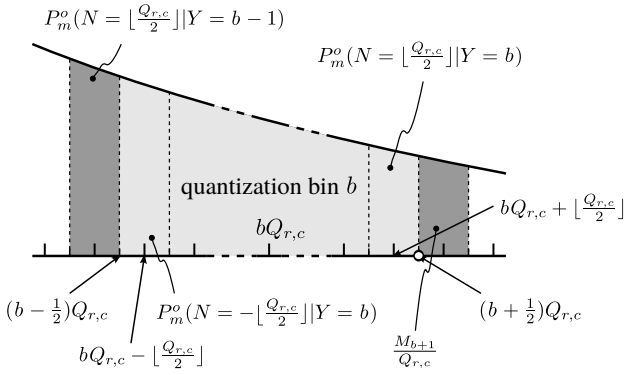

(a) $Q_{r,c}$ is an odd number

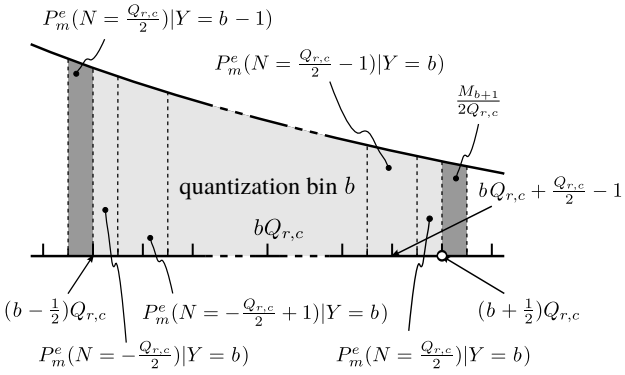

(b) $Q_{r,c}$ is an even number

Figure 3: For the quantization bin $b > 0$, the probability of DCT coefficient falling in the leftmost integer bin should be no bigger than that in the rightmost integer bin of the neighboring quantization bin $b-1$, meanwhile the probability of coefficients falling in the rightmost integer bin of quantization bin b should be no smaller than that in the leftmost integer bin of quantization bin $b+1$.

As illustrated in Figure 3 (a)-(b), we consider a quantization bin $b > 0$, when $Q_{r,c}$ is an odd number and an even number, respectively. The probability of DCT coefficient falling in the leftmost integer bin of quantization bin b should be no bigger than that in the rightmost integer bin of quantization bin $b-1$. Meanwhile, the probability of DCT coefficient falling in the rightmost integer bin of quantization bin b should be no smaller than that in the leftmost integer bin of quantization bin $b+1$. As the building of the dithering signal model is an iterative procedure, the distribution of the dithering signal N in the quantization bin $b-1$ has already been estimated in the last iteration. Hence, $P_m^o(N=n|Y=b-1)$ or $P_m^e(N=n|Y=b-1)$ is known. Moreover, for the quantization bin $b+1$, its dithering signal is assumed to follow a uniform distribution for the moment. Therefore, when $Q_{r,c}$ is an odd number, the constraints that λ_b^- and λ_b^+ can be respectively found by solving:

$$\begin{aligned}\lambda_b^- = &\underset{10^{-3}\le\lambda\le\lambda_{b-1}}{\arg\min}\ \lambda \\ \text{subject to: } &\begin{cases} P_m^o\left(N=-\left\lfloor\frac{Q_{r,c}}{2}\right\rfloor|Y=b\right)\times M_b \le P_m^o\left(N=\left\lfloor\frac{Q_{r,c}}{2}\right\rfloor|Y=b-1\right)\times M_{b-1} \\ P_m^o\left(N=\left\lfloor\frac{Q_{r,c}}{2}\right\rfloor|Y=b\right)\times M_b \ge \frac{M_{b+1}}{Q_{r,c}}, \end{cases}\end{aligned} \tag{8}$$

and

$$\lambda_b^+ = \underset{10^{-3}\le\lambda\le\lambda_{b-1}}{\arg\max} \quad \lambda$$
$$\text{subject to: } \begin{cases} P_m^o\left(N = -\left\lfloor\frac{Q_{r,c}}{2}\right\rfloor|Y=b\right)\times M_b \le P_m^o(N = \left\lfloor\frac{Q_{r,c}}{2}\right\rfloor|Y=b-1)\times M_{b-1} \\ P_m^o\left(N = \left\lfloor\frac{Q_{r,c}}{2}\right\rfloor|Y=b\right)\times M_b \ge \frac{M_{b+1}}{Q_{r,c}}. \end{cases} \tag{9}$$

Similarly, λ_b^- and λ_b^+ are respectively defined as:

$$\lambda_b^- = \underset{10^{-3}\le\lambda\le\lambda_{b-1}}{\arg\min} \quad \lambda$$
$$\text{subject to: } \begin{cases} P_m^e\left(N = -\frac{Q_{r,c}}{2}+1|Y=b\right)\times M_b \le P_m^e\left(N = -\frac{Q_{r,c}}{2}|Y=b\right)\times M_b + P_m^e\left(N = \frac{Q_{r,c}}{2}|Y=b-1\right)\times M_{b-1} \\ P_m^e\left(N = \frac{Q_{r,c}}{2}-1|Y=b\right)\times M_b \ge P_m^e\left(N = \frac{Q_{r,c}}{2}|Y=b\right)\times M_b + \frac{M_{b+1}}{2Q_{r,c}}, \end{cases} \tag{10}$$

and

$$\lambda_b^+ = \underset{10^{-3}\le\lambda\le\lambda_{b-1}}{\arg\max} \quad \lambda$$
$$\text{subject to: } \begin{cases} P_m^e\left(N = -\frac{Q_{r,c}}{2}+1|Y=b\right)\times M_b \le P_m^e\left(N = -\frac{Q_{r,c}}{2}|Y=b\right)\times M_b + P_m^e\left(N = \frac{Q_{r,c}}{2}|Y=b-1\right)\times M_{b-1} \\ P_m^e\left(N = \frac{Q_{r,c}}{2}-1|Y=b\right)\times M_b \ge P_m^e\left(N = \frac{Q_{r,c}}{2}|Y=b\right)\times M_b + \frac{M_{b+1}}{2Q_{r,c}}, \end{cases} \tag{11}$$

when $Q_{r,c}$ is an even number.

In other words, using a numerical method, λ_b^- and λ_b^+ are found respectively as the smallest and largest number in the interval $[10^{-3}, \lambda_{b-1}]$ satisfying certain constraints. Note that λ_{b-1} is estimated from the last iteration. If λ_b^- and λ_b^+ cannot be found, the uniform model will be adopted for the current and following quantization bin(s).

3.3 In the quantization bin $b < 0$

For the quantization bin $b < 0$, the procedure of building the dithering signal model is very similar to that for quantization bin $b > 0$. For the sake of simplicity, we do not present the details here, but only give the equations for searching λ_b^- and λ_b^+, that are:

$$\lambda_b^- = \underset{10^{-3}\le\lambda\le\lambda_{b+1}}{\arg\min} \quad \lambda$$
$$\text{subject to: } \begin{cases} P_m^o\left(N = -\left\lfloor\frac{Q_{r,c}}{2}\right\rfloor|Y=b\right)\times M_b \ge \frac{M_{b-1}}{Q_{r,c}} \\ P_m^o\left(N = \left\lfloor\frac{Q_{r,c}}{2}\right\rfloor|Y=b\right)\times M_b \le P_m^o(N = -\left\lfloor\frac{Q_{r,c}}{2}\right\rfloor|Y=b+1)\times M_{b+1}, \end{cases} \tag{12}$$

and

$$\lambda_b^+ = \underset{10^{-3}\le\lambda\le\lambda_{b+1}}{\arg\max} \quad \lambda$$
$$\text{subject to: } \begin{cases} P_m^o\left(N = -\left\lfloor\frac{Q_{r,c}}{2}\right\rfloor|Y=b\right)\times M_b \ge \frac{M_{b-1}}{Q_{r,c}} \\ P_m^o\left(N = \left\lfloor\frac{Q_{r,c}}{2}\right\rfloor|Y=b\right)\times M_b \le P_m^o\left(N = -\lfloor\frac{Q_{r,c}}{2}\rfloor|Y=b+1\right)\times M_{b+1}, \end{cases} \tag{13}$$

when $Q_{r,c}$ is an odd number, or:

$$\lambda_b^- = \underset{10^{-3}\le\lambda\le\lambda_{b+1}}{\arg\min} \quad \lambda$$
$$\text{subject to: } \begin{cases} P_m^e\left(N = -\frac{Q_{r,c}}{2}+1|Y=b\right)\times M_b \ge P_m^e\left(N = -\frac{Q_{r,c}}{2}|Y=b\right)\times M_b + \frac{M_{b-1}}{2Q_{r,c}} \\ P_m^e\left(N = \frac{Q_{r,c}}{2}-1|Y=b\right)\times M_b \le P_m^e\left(N = \frac{Q_{r,c}}{2}|Y=b\right)\times M_b + P_m^e\left(N = -\frac{Q_{r,c}}{2}|Y=b+1\right)\times M_{b+1}, \end{cases} \tag{14}$$

and

$$\lambda_b^+ = \underset{10^{-3}\le\lambda\le\lambda_{b+1}}{\arg\max} \quad \lambda$$
$$\text{subject to: } \begin{cases} P_m^e\left(N = -\frac{Q_{r,c}}{2}+1|Y=b\right)\times M_b \ge P_m^e\left(N = -\frac{Q_{r,c}}{2}|Y=b\right)\times M_b + \frac{M_{b-1}}{2Q_{r,c}} \\ P_m^e\left(N = \frac{Q_{r,c}}{2}-1|Y=b\right)\times M_b \le P_m^e\left(N = \frac{Q_{r,c}}{2}|Y=b\right)\times M_b + P_m^e\left(N = -\frac{Q_{r,c}}{2}|Y=b+1\right)\times M_{b+1}, \end{cases} \tag{15}$$

when $Q_{r,c}$ is an even number.

4 Example DCT histogram results of our JPEG forgery

Figure 4 shows the DCT histograms of subbands $(2,2)$, $(6,4)$, $(3,7)$, and $(8,8)$ of the JPEG forgery (whose close-up image is shown in the Fig. 9-(d) in the paper) created using the proposed JPEG anti-forensic method. It can be seen that no noticeable artifacts appear in the DCT histogram.

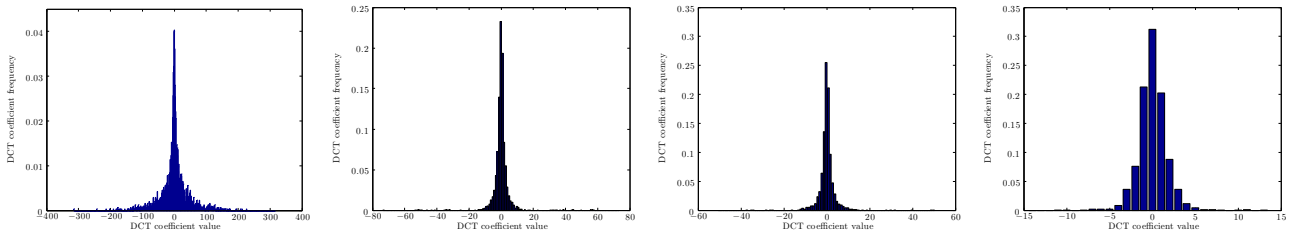

(a) $(2,2)$ (b) $(6,4)$ (c) $(3,7)$ (d) $(8,8)$

Figure 4: Example DCT histograms of the JPEG forgery created using the proposed JPEG anti-forensic method. No noticeable comb-like DCT quantization artifacts appear.

5 Comparing intermediate images

Table 1: From the 2nd to the 8th columns, the minimal decision error for different kinds of images when tested against different JPEG forensic detectors is listed; the image quality (with $\mathcal{I}$ as the reference) comparison is reported in the last two columns. Results are achieved by test on UCID-v2 corpus

	K_F [3]	K_{Luo} [4]	K^Q_{Luo} [4]	K_V [7]	K_L [8]	K^1_U [12]	K^2_U [12]	PSNR	SSIM
$\mathcal{J}$	0.0082	0	0.0052	0.0108	0.0374	0.0396	0.1928	37.0076	0.9920
$\hat{\mathcal{F}}_b$	0.2948	0.4716	0.5000	0.1966	0.0893	0.3576	0.4447	36.6628	0.9891
$\hat{\mathcal{F}}_{bq}$	0.1562	0.4817	0.4585	0.2182	0.0441	0.2556	0.3819	35.9023	0.9871
$\mathcal{F}$	0.4477	0.3972	0.4996	0.3756	0.5000	0.4208	0.4701	35.9019	0.9866

In this section, we compare the two intermediate images, that are $\hat{\mathcal{F}}_b$ after the first-round TV-based deblocking, and $\hat{\mathcal{F}}_{bq}$ after the perceptual DCT histogram smoothing, with the JPEG image $\mathcal{J}$ and our final JPEG forgery $\mathcal{F}$.

As an extension of the Table V in the paper, Table 1 reports the anti-forensic performance against various JPEG forensic detectors, and the image quality for the above four kinds of images. Results are achieved by conducting test on UCID-v2 corpus. It can be seen that after the first-round TV-based deblocking, the anti-forensic performance of $\hat{\mathcal{F}}_b$ against JPEG blocking artifact detectors K_F, K^1_U, and K^2_U has been improved, though not as satisfactory as our final result $\mathcal{F}$. Please note that it is important to explicitly smooth the DCT histograms; otherwise the unfilled gaps in DCT histograms might be exposed, for example by the double JPEG compression detector in [19] (see the Sec. VI-A and the Fig. 10 in the paper, the result of our previously proposed method [12]). However, the cost is that, after the perceptual DCT histogram smoothing, some unnatural noise and blocking artifacts must have been introduced in $\hat{\mathcal{F}}_{bq}$. This is reflected by the minimal decision error change for detectors K_F, K^1_U, and K^2_U, and by the image quality decrease of $\hat{\mathcal{F}}_{bq}$ compared with $\hat{\mathcal{F}}_b$. Furthermore, with the second-round TV-based deblocking and *de-calibration* operations, our final JPEG forgery $\mathcal{F}$ is able to achieve satisfactory overall anti-forensic performance, with a very slight image quality loss compared to $\hat{\mathcal{F}}_{bq}$.

Overall, by removing JPEG artifacts alternatively in the spatial and in the DCT domains, we are able to drag the processed image out from the detection regions of multiple detectors working in different domains, at the cost of a reasonable image quality loss.

6 Hiding traces of aligned double JPEG compression

In [17], Pevny and Fridrich proposed a method using the SVM with feature vectors formed by DCT histograms in the low-frequency subbands to classify single and double JPEG compressed images. For constructing the feature vector, they consider 9 low-frequency AC subbands, and for each of them a 16-bin histogram is computed. The 144-dimensional feature vectors are then fed to an SVM.

In order to train the SVM-based A-DJPG compression detector [17], each image in UCIDTrain is firstly JPEG compressed with the primary quality factor QF_1 and then compressed again with the secondary quality

factor $QF_2 \neq QF_1$ to create the A-DJPG compressed images. Here, $QF_1 \in \{50, 56, 63, 69, 81, 88, 94\}$, and $QF_2 = 75$. The single JPEG compressed images are created by JPEG compressing the original uncompressed images with QF_2. Then we have $7 \times 669 + 669 = 5352$ images for training the detector, using LIBSVM [41].

Each UCIDTest image is firstly JPEG compressed with QF_1, and then compressed again with QF_2 to create the A-DJPG compressed images. During the two JPEG compressions, anti-forensic operations may occur. Meanwhile, each UCIDTest image is JPEG compressed once with QF_2 for creating the single JPEG compressed image. For forensic testing, we create 7 datasets each of which has 5352 images as well. The name of the dataset follows the pattern **A-DJPG-*R***, as explained at the beginning of the Sec. VI of the paper.

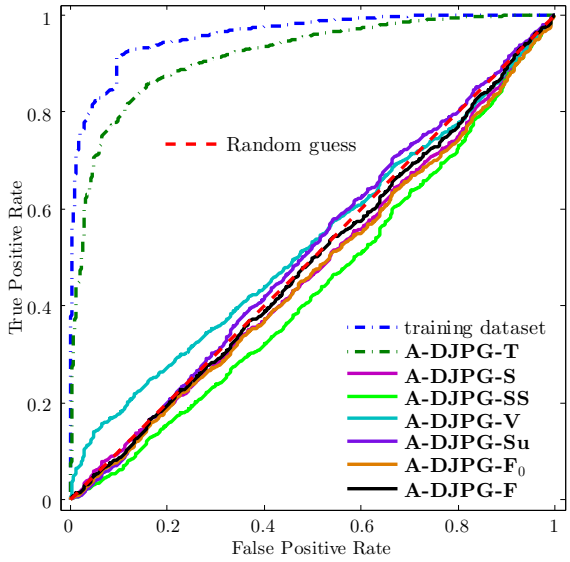

Figure 5: ROC curves of **A-DJPG-*R*** under the testing of the SVM-based A-DJPG compression detector [17]. Results are achieved by test on UCIDTrain and UCIDTest.

The ROC curves in Figure 5 show that the proposed method successfully masks the presence of double JPEG compression artifacts. The minimal decision error of the A-DJPG compression detector [17] is increased to 0.4985 for **A-DJPG-F** from 0.0915 for the training dataset and 0.1498 for **A-DJPG-T**. Other state-of-the-art JPEG anti-forensic methods [5], [6], [9], [12], [13] achieve similar anti-forensic performance, however with higher image quality loss than ours, as reported in Table 2. Among different anti-forensic double JPEG compressed images, our forgeries have the highest visual quality (with the uncompressed image as the reference).

Table 2: Image quality (with the uncompressed image as the reference) comparison of (anti-forensic) double JPEG compressed images created from UCIDTest for different datasets **A-DJPG-*R***

	-T	**-S**	**-SS**	**-V**	**-Su**	**-F$_0$**	**-F**
PSNR	34.9854	32.7570	30.1157	32.6701	30.7715	34.0804	34.3273
SSIM	0.9881	0.9685	0.9432	0.9762	0.9653	0.9802	0.9823

7 Fooling JPEG artifact based image forgery localization

Bianchi and Piva [16] derived a likelihood-map indicating the probability for each 8×8 block of being double JPEG compressed, under the hypothesis of the presence of A-DJPG or NA-DJPG compression artifacts in the tampered image.

We randomly select 100 images from UCIDTest for forensic testing and we call this small dataset UCIDTest100. Following [16], we first compress each UCIDTest100 image with QF_1; the resulting image is partly replaced using the original uncompressed image, and then compressed again with QF_2. After the primary JPEG compression, image cropping and/or anti-forensics may occur. In total, 42 datasets are created considering different scenarios. We name the dataset as **LOC-*E*-DJPG-*K*/*L*-*R***, where the italic letters may change to represent different scenarios. ***E*** can be '**A**', or '**NA**'. '**NA**' indicates that before the second compression the image is cropped by a random shift $(i, j) \neq (0, 0), 0 \leq i, j \leq 7$; whereas '**A**' means there is no image cropping happening. ***K*/*L*** indicates how much portion of the image has undergone double JPEG compression, which also implies how much portion of the image has been replaced by the original uncompressed image before the second JPEG compression. When ***K*/*L*** is '**1/2**', it indicates the left half of the image is replaced using the original image; when

$\boldsymbol{K/L}$ is '**15/16**', the central 1/16 portion of the image is replaced; when $\boldsymbol{K/L}$ is '**1/16**', the whole image except its central 1/16 portion is replaced. In all datasets, QF_1 and QF_2 are taken from $\{50, 56, 63, 69, 75, 81, 88, 94\}$ and $\{50, 56, 63, 69, 75, 81, 88, 94, 100\}$, respectively. Therefore each dataset has $8 \times 9 \times 100 = 7200$ images.

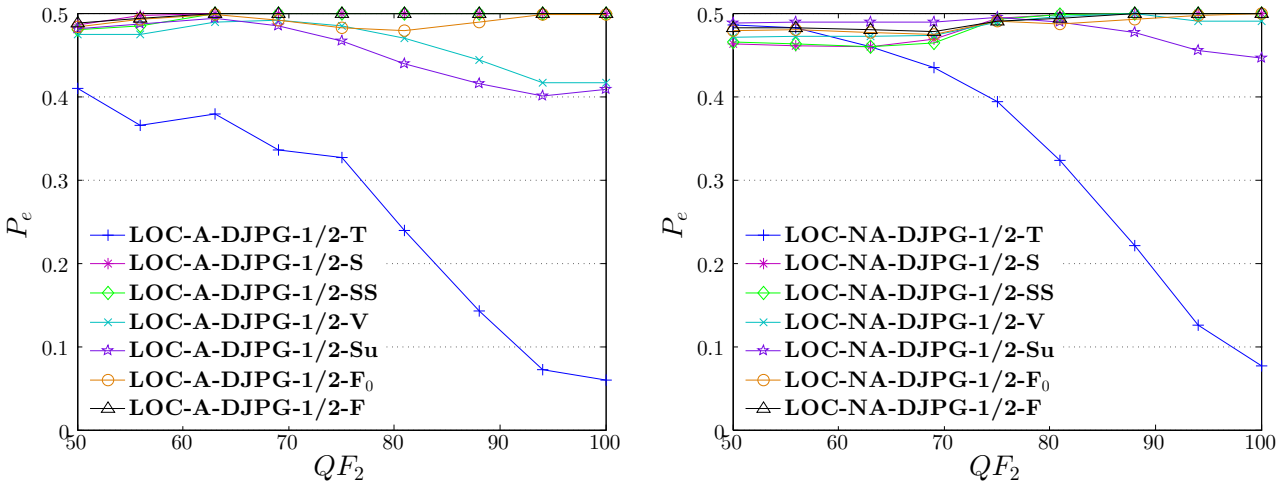

(a) **LOC-A-DJPG-1/2-*R***

(b) **LOC-NA-DJPG-1/2-*R***

Figure 6: Average minimal decision error as a function of QF_2 of the forgery localization detector [16], when tested on **LOC-*E*-DJPG-1/2-*R***, created from UCIDTest100.

Figure 6 shows the average minimal decision error averaged over all possible QF_1 (under a fixed value of QF_2) achieved by the detector [16] for the scenarios where $\boldsymbol{K/L}$ is '**1/2**', for different kinds of images. Note that the results shown here are computed from the standard map instead of the simplified map (see [16] for details). The blue curves demonstrate the effectiveness of the detector when no JPEG anti-forensics is applied after the first compression. With the help of JPEG anti-forensics, the forgery localization detector [16] is no longer reliable. Similar results are obtained for scenarios where $\boldsymbol{K/L}$ is '**15/16**' or '**1/16**'. As reported in Tables 3-4, our forgeries again achieve the best image visual quality among all kinds of forgeries.

Table 3: Image quality (with the uncompressed image as the reference) comparison of (anti-forensic) double JPEG compressed images created from UCIDTest100 for different datasets **LOC-A-DJPG-1/2-*R***

	-T	**-S**	**-SS**	**-V**	**-Su**	**-F$_0$**	**-F**
PSNR	36.4957	34.8282	32.7239	34.7915	33.2092	35.7707	35.9792
SSIM	0.9899	0.9830	0.9686	0.9853	0.9785	0.9857	0.9869

Table 4: Image quality (with the uncompressed image as the reference) comparison of (anti-forensic) double JPEG compressed images created from UCIDTest100 for different datasets **LOC-NA-DJPG-1/2-*R***

	-T	**-S**	**-SS**	**-V**	**-Su**	**-F$_0$**	**-F**
PSNR	36.2184	34.5754	32.6795	34.4153	33.1158	35.6269	35.8131
SSIM	0.9517	0.9186	0.9142	0.9290	0.9321	0.9448	0.9471

In Secs. 6-7 and the Sec. VI-A of the paper, we have shown the effectiveness of the proposed JPEG anti-forensic method in disguising double JPEG compression artifacts. Obviously, our method is not the only JPEG anti-forensic method which is able to achieve this goal. The advantage of our method is that the created anti-forensic double JPEG compressed images have the highest visual quality among all the six kinds of forgeries (see Tables 2-4 and the Table VII of the paper). Hence, our JPEG anti-forensic method is again proven to achieve a better trade-off between the forensic undetectability and the image quality, in three applications of hiding double JPEG compression artifacts.